Sonochemical effects on single-bubble sonoluminescence

Li Yuan*
LSEC and Institute of Computational Mathematics, Academy of Mathematics and Systems Science, Academia Sinica, Beijing 100080, People's Republic of China
(Dated: January 13, 2005)

A refined hydro-chemical model for single-bubble sonoluminescence is presented. The processes of water vapor evaporation and condensation, mass diffusion, and chemical reactions are taken into account. Numerical simulations of Xe-, Ar- and He-filled bubbles are carried out. The results show that the trapped water vapor in conjunction with its endothermic chemical reactions significantly reduces the temperature within the bubble so that the degrees of ionization are generally very low. The chemical radicals generated from water vapor are shown to play an increasingly important role in the light emission from Xe to He bubbles. Light spectra and pulses computed from an optically thin model and from an essentially blackbody model are compared with recent experimental results. It is found that the results of the blackbody model generally match better with the experiment ones than those of the optically thin model. Suggestions on how to reconcile the conflict are given.

PACS numbers: 78.60.Mq, 47.40.Fw, 43.25.+y

I. INTRODUCTION

The discovery that acoustic energy can be converted to light through an oscillating air bubble trapped in water [1] has triggered extensive studies on single-bubble sonoluminescence (SBSL) (cf. reviews in [2, 3]). Under certain conditions, a stable and regular flash of blue-white light with a width of about 40-350 ps is emitted during the violent collapse of the bubble in each acoustic cycle [4–6]. Among many candidate mechanisms of SBSL light emission, the model that identified SBSL light emission as thermal bremsstrahlung and recombination radiation from an optically thin bubble seemed to predict the widths, shapes and spectra of the emitted light fairly well under certain simplified hydrodynamic frameworks [7–9]. Similar models included those which used finite opacity to define a variable blackbody core [10, 11], or a sheer blackbody model assuming a fix-sized emission core [12]. However, different approximations in modelling the physical-chemical processes, and particularly, uncertainties under the extreme conditions inside a sonoluminescing (SL) bubble, may give diverse predictions that plague the validity of a light emission model. Therefore, more realistic hydrodynamic-chemical modelling and more critical tests of the light emission models under the refined hydro-chemical framework are necessary.

Past studies delineated the important effects of diffusive transport, surface tension and compressibility of the surrounding liquid on SBSL [13–15]. Earlier studies considered the influence of evaporation-condensation phenomena on the bubble dynamics [16, 17]. Recently, the study of sonochemsitry was extending from lower temperature to higher temperature situations to approach SL problems [18–20]. Sochard *et al.* [21] and Gong *et al.* [19] coupled the bubble dynamics with the water vapor dissociations. Yasui [18] presented a model of SBSL that accounts for evaporation-condensation process at the bubble interface and water vapor chemical reactions. It was later stressed by Storey and Szeri [22] and others [23–26] that water vapor reduce the temperatures inside the SL bubble significantly by reducing the compression heating of the mixture and through primarily endothermic chemical reactions. In some of these models, spatial uniformity of the bubble interior was assumed and inter-molecular mass diffusion was not taken into account. As a consequence, such models often underpredicted the amount of trapped water vapor during the rapid collapse.

In the full hydro-chemical numerical study by Storey and Szeri [22], the consequences of water vapor inside strongly forced argon bubbles were investigated in detail. The interaction of nonlinearity of the volume oscillations, mass diffusion, and nonequilibrium phase change at the bubble wall resulted in excess water vapor trapped in the bubble during the violent collapse. The amount of trapped water vapor was more than that predicted by the simple model [18]. Akhatov *et al.* [27] accounted for the occurrence of supercritical conditions of condensation and studied laser-induced cavitation bubbles. The effects of water vapor diffusion in different noble gas bubbles were studied by Xu *et al.* [28], where shock waves were found to occur only in Xe bubbles. More recently, Toegel *et al.* [25] studied the effects of the highly compressed conditions of SL bubbles on chemical equilibrium constants. They showed that high

*Electronic address: lyuan@lsec.cc.ac.cn

temperatures could be recovered due to the suppressed water vapor dissociations. In spite of the progress made, the direct consequence of sonochemistry on existing popular light emission models is to be revealed.

In this paper, we present a refined hydrodynamic model taking into account the chemical reactions and ionizations of the noble gas and water vapor mixture. The model is an extension of our previous ones [11, 14, 29]. As done in [11], the multispecies Navier-Stokes (NS) equations for the gas mixture in the bubble interior are coupled with a proper form of the Rayleigh-Plesset (RP) equation for the bubble wall, including the effects of liquid compressibility and heat transfer. The new feature of the model is that the nonequilibrium processes of evaporation and condensation, species diffusion, noble gas exchange between the bubble and the surrounding liquid, and dissociations of water vapor and ionizations of atomic species inside the bubble are all taken into account. The numerical scheme for solving the hydrodynamic equations is modified to be a semi-implicit one which allows for better numerical stability than original explicit scheme in [14].

Detailed formulae in Eulerian framework are given. Numerical simulations are carried out for bubbles of He, Ar, or Xe gases. The effects of sonochemistry on current light-emitting models of SBSL [8, 11, 23] are studied in detail through comparison with a calibrated experiment [12]. The main conclusions are: (i) the chemical reactions reduce the temperature within the bubble to such an extent that the degrees of ionization are generally very low; (ii) shock waves do not appear in He or Ar bubbles in the stable SBSL regime, but can occur in Xe bubbles only at higher driving pressures; (iii) chemical radicals generated from the water vapor contribute dominantly to the light emission of He bubbles; (iv) based on computed photon absorption coefficients, the popular optically thin thermal radiation model is less able to fit the experimental light spectra and pulse widths than an essentially blackbody radiation model with an assumed dynamic blackbody core. Some suggestions on how to reconcile the contradiction are outlined.

II. HYDRODYNAMIC MODEL

In this section, we extend our previous hydrodynamic model [11, 14] to include processes of evaporation-condensation on the wall and chemical reactions inside the bubble. The bubble is still assumed to be spherically symmetric and is composed of the mixture of noble gas, water vapor and reaction products. In addition to the NS and RP equations, the equations for the mass concentration of the dissolved noble gas and for the temperature of the surrounding water are also solved.

A. Gas dynamics in the bubble

1. The NS equations

The bubble is assumed to contain N-species gas mixture: a noble gas and its ions, water vapor and its reaction products ($N = 13$: Ar, Ar^+, Ar^{2+}, Ar^{3+}, H_2O, OH, H, H^+, O, O^+, H_2, O_2, e^-). Chemical reactions of the water vapor and ionizations of atomic species (Ar, H and O) are considered. The dynamics inside the bubble is described by the compressible NS equations, which represent the conservation of mass, momentum and energy. They can be written into a "conservative" form in the spherical coordinates:

$$\frac{\partial \mathbf{Q}}{\partial t} + \frac{\partial \mathbf{F}}{\partial r} = \mathbf{H} + \frac{1}{r^2}\frac{\partial r^2 \mathbf{F}_\nu}{\partial r} + \mathbf{M}_\nu + \mathbf{S}, \tag{1}$$

with

$$\mathbf{Q} = \begin{bmatrix} \rho_1 \\ \vdots \\ \rho_{_N} \\ \rho u \\ \rho E \end{bmatrix}, \quad \mathbf{F} = \begin{bmatrix} \rho_1 u \\ \vdots \\ \rho_{_N} u \\ \rho u^2 + P \\ u(\rho E + P) \end{bmatrix}, \quad \mathbf{H} = -\frac{2u}{r}\begin{bmatrix} \rho_1 \\ \vdots \\ \rho_{_N} \\ \rho u \\ \rho E + P \end{bmatrix},$$

$$\mathbf{F}_\nu = \begin{bmatrix} -J_1 \\ \vdots \\ -J_{_N} \\ \tau_{rr} \\ u\tau_{rr} + q \end{bmatrix}, \quad \mathbf{M}_\nu = \begin{bmatrix} 0 \\ \vdots \\ 0 \\ -(\tau_{\theta\theta} + \tau_{\phi\phi})/r \\ 0 \end{bmatrix}, \quad \mathbf{S} = \begin{bmatrix} \dot{\omega}_1 \\ \vdots \\ \dot{\omega}_{_N} \\ 0 \\ 0 \end{bmatrix}, \tag{2}$$

and

$$\rho = \sum_{i=1}^{N} \rho_i, \quad E = e + \frac{u^2}{2}, \quad e = \sum_{i=1}^{N} e_i, \quad \tau_{rr} = -2\tau_{\theta\theta} = -2\tau_{\phi\phi} = \frac{4\mu}{3}\left(\frac{\partial u}{\partial r} - \frac{u}{r}\right),$$

$$q = \lambda \frac{\partial T}{\partial r} - \sum_{i=1}^{N} J_i h_i, \quad J_i = -\rho D_i^M \frac{M_i}{\bar{M}} \left[\frac{\partial X_i}{\partial r} + (X_i - Y_i)\frac{\partial \ln P}{\partial r} + K_i^T \frac{\partial \ln T}{\partial r}\right], \tag{3}$$

$$Y_i = \frac{\rho_i}{\rho}, \quad X_i = Y_i \frac{\bar{M}}{M_i}, \quad \bar{M} = \frac{1}{\sum_{i=1}^{N} \frac{Y_i}{M_i}}, \quad D_i^M = \frac{1 - Y_i}{\sum_{j \neq i}^{N} X_j / D_{ij}}, \quad h_i = e_i + \frac{P_i}{\rho_i},$$

where ρ_i is density of species i, ρ is the total density of gas mixture, P is the pressure, T is the temperature, u is the mass averaged velocity, e is the total internal energy of the mixture, e_i and h_i are the internal energy and enthalpy of species i, respectively, P_i is the partial pressure, μ and λ are the viscosity and the thermal conductivity of the mixture, respectively, Y_i and X_i are the mass fraction and mole fraction of species i, respectively, M_i is the molar mass of species i, $\bar{M}$ is the mean molar mass of the mixture, D_{ij} is the binary diffusion coefficient between species i and j, D_i^M is the mean diffusion coefficient of species i into the mixture, K_i^T is the thermal diffusion ratio, τ_{rr} is the normal stress, J_i is the mass diffusion flux that must satisfy $\sum_{i=1}^{N} J_i = 0$, and $\dot{\omega}_i$ is the net mass production rate due to chemical reactions and ionizations that satisfies $\sum_{i=1}^{N} \dot{\omega}_i = 0$. Use of the mean diffusion coefficient is a practical approximation for computational efficiency [22, 30]. However, to ensure global mass conservation, a correction diffusion flux $J_i^c = \rho_i \sum_{i=1}^{N} D_i^M \frac{M_i}{\bar{M}} \left[\frac{\partial X_i}{\partial r} + (X_i - Y_i)\frac{\partial \ln P}{\partial r} + K_i^T \frac{\partial \ln T}{\partial r}\right]$, is added to the flux J_i in (3), as recommended by Ref. [30]. It can be easily shown that the resulting J_i satisfies $\sum_{i=1}^{N} J_i = 0$.

2. Transport properties, equation of state and thermodynamic properties

The individual transport properties (viscosity μ_i, thermal conductivity λ_i, thermal diffusion ratio k_i^T and binary diffusion coefficient D_{ij}) are generally calculated based on Chapman-Enskog theory [31–33]. However, the transport properties of the gas mixture, μ, λ are determined by some empirical combination rules such as Wilke's semi-empirical formula [32]. There is also difficulty in describing individual μ_i and D_{ij} for some reaction products due to lack of data. We shall let unavailable μ_i and D_{ij} equal to other known ones, e.g., $\mu_{\mathrm{OH}} = \mu_{\mathrm{H_2O}}, \mu_{\mathrm{H}} = \mu_{\mathrm{H_2}}$. Collision cross-sections of ions, electron and some radical species that are not available in [31, 32] can be determined using NASA temperature dependent polynomial fitting [34]. Once μ_i is known, λ_i is obtained by modified Eucken model [31, 32]. The trouble lies in the determination of k_i^T. In this regard, we only take into account the thermal diffusion between the most ample species, i.e. between the noble gas and the water vapor, since thermal diffusion is only important in slow stage other than collapse [22, 33]. The high pressure corrections [32] are applied to μ_i and λ_i similar to what Xu [28] did. The transport properties of the mixture, μ and λ, are obtained by using Wilke's semi-empirical formula

$$\mu = \sum_{i=1}^{N} \left(\frac{X_i \mu_i}{\sum_{j=1}^{N} X_j \phi_{ij}}\right), \tag{4}$$

$$\lambda = \sum_{i=1}^{N} \left(\frac{X_i \lambda_i}{\sum_{j=1}^{N} X_j \phi_{ij}}\right), \tag{5}$$

where

$$\phi_{ij} = \left[1 + \left(\frac{\mu_i}{\mu_j}\right)^{1/2} \left(\frac{M_j}{M_i}\right)^{1/4}\right]^2 \left[\sqrt{8}\left(1 + \frac{M_i}{M_j}\right)^{1/2}\right]^{-1}. \tag{6}$$

The hydrodynamics of the bubble is affected by the equation of state. Here the gas mixture is modelled by a hard-core van der Waals equation of state that has the excluded volume but ignores the van der Waals force as previous authors did [35]

$$P = \sum_{i=1}^{N} P_i = \frac{\rho R T}{1 - b\rho} = P(T, \rho_1, \cdots, \rho_N), \tag{7}$$

where $R = \sum_{i=1}^{N} Y_i R_i, R_i = \frac{R_u}{M_i}$, R_u is the universal gas constant, $b = \sum_{i=1}^{N} Y_i b_i$ is a simple combination of b_i, where b_i is the van der Waals excluded volume in m^3/kg. The values of $\tilde{b}_i = b_i M_i$ (cm^3/mol) are computed by $\tilde{b} = \frac{RT_c}{8P_c}$ where T_c and P_c are critical temperature and pressure [32]. When critical point parameters are not available, they are taken as 4 times the spherical volume of the atomic or ionic radius.

A well-posedness of equation closure requires $P = f(e, \rho_1, \cdots, \rho_N)$, therefore, T must be solved for from the given energy relation

$$E = e + \frac{u^2}{2}, \qquad e = \sum_{i=1}^{N} Y_i \left(C_{Vi} R_i T + e_i^0 \right) + \sum_{i=\text{molecues}} Y_i e_i^V + \sum_{i=\text{ions}} Y_i e_i^I, \tag{8}$$

where the internal energy is divided into the translational and rotational, the vibrational, and the ionization parts. The coefficient of specific heat at constant volume, C_{Vi} is approximately assumed as follows [18]: $C_{Vi} = \frac{3}{2}$ for monatomic gases such as Ar, Ar^+, H, O; $C_{Vi} = \frac{5}{2}$ for diatomic gases such as OH, H_2, O_2, and $C_{Vi} = \frac{6}{2}$ for other gases. e_i^0 is the reference energy per unit mass at 0 K, e_i^V is the vibrational energy per unit mass for molecules species, and e_i^I is the ionization energy per unit mass for ion species. The reference energy e_i^0 is evaluated from standard heat of formation at 298 K [36].

3. Chemical kinetics

The chemical kinetics consists of the reaction mechanism and determines the net production rate of each species. The present reaction scheme includes both chemical reactions of water vapor and ionizations of monatomic species. For the chemical reactions of water vapor, we use the mechanism that were described in detail in [37]. Only a subset consisting of 8 forward and reverse elementary reactions is used, corresponding to the first eight ones used by Yasui [18]. The first 19 reactions of [18] with additional species (HO_2, H_2O_2) were also tried but the results were found to be a little different from the 8 reactions. The collisional ionizations and recombinations are considered only for three monatomic species: noble gas, H and O. The reasons to choose H and O atoms are that they are quite ample in the water vapor dissociations, have lower ionization potentials, and can be treated using previous rate formulae [38]. Although H_2O and OH are almost as ample as H and O, and have lower ionization potentials too, their ionization processes are believed to be more complicated than a single atom, thus are not accounted for in this study. The maximum ionization level is taken as 3 for a noble gas, and 1 for H or O atom. The net production rate due to chemical reactions of the water vapor is determined via the law of mass action:

$$\dot{\omega}_k = M_k \sum_{i=1}^{N_r} \left(\nu''_{ki} - \nu'_{ki} \right) q_i, \tag{9}$$

$$q_i = k_{f_i} \prod_{k=1}^{N} \left(\frac{\rho_k}{M_k} \right)^{\nu'_{ki}} - k_{b_i} \prod_{k=1}^{N} \left(\frac{\rho_k}{M_k} \right)^{\nu''_{ki}}, \tag{10}$$

where $\nu_{ki} = \nu''_{ki} - \nu'_{ki}$, N_r is the total number of elementary reactions. The forward and backward reaction rate constants for the ith reaction, k_{f_i} and k_{b_i}, are given in Arrhenius form

$$k_{f_i} = A_i^f T^{B_i^f} \exp\left(-C_i^f / T \right), \quad k_{b_i} = A_i^b T^{B_i^b} \exp\left(-C_i^b / T \right). \tag{11}$$

Since the above rate constants as given in [37] are based on ideal gas, the van der Waals gas modification suggested by Togel *et al.* [25] is used. As they hinted, we can derive the equilibrium constant based on fugacity for a van der Waals gas [32]

$$K_{f_i} = \frac{K_{p_i}^{\text{ideal}}}{(1 - b\rho)^{\sum_{k=1}^{N} \nu_{ki}} \exp\left(-\frac{\sum_{k=1}^{N} \nu_{ki} b_k \rho_k}{1 - b\rho} \right)}. \tag{12}$$

Let the corrected $k'_{f_i} = k_{f_i}$ frozen, we can obtain the corrected k'_{b_i} as

$$k'_{b_i} = \frac{k'_{f_i}}{K_{p_i}^{\text{ideal}}} = \frac{k_{b_i}}{(1 - b\rho)^{\sum_{k=1}^{N} \nu_{ki}} \exp\left(-\frac{\sum_{k=1}^{N} \nu_{ki} b_k \rho_k}{1 - b\rho} \right)}. \tag{13}$$

We will use k'_{f_i} and k'_{b_i} in Eq.(10). The Effects of the above modification were pointed out in [25], which suppress water vapor dissociation to some extent when compared with the raw rate constants k_{f_i} and k_{b_i}.

When involving the third-body reaction, the net rate of progress q_i in (10) is modified as

$$q_i = \left[\sum_{k=1}^{N} Z_{k,i}\left(\frac{\rho_k}{M_k}\right)\right]\left[k'_{f_i}\prod_{k=1}^{N}\left(\frac{\rho_k}{M_k}\right)^{\nu'_{ki}} - k'_{b_i}\prod_{k=1}^{N}\left(\frac{\rho_k}{M_k}\right)^{\nu''_{ki}}\right], \tag{14}$$

where $Z_{k,i}$ is the third-body enhanced coefficient. Due to length limitation, the detailed formulae for net production rates and rate constants of collisional ionization, recombination and three-body recombination are not given here. One can refer to [11, 38] for detail.

4. Mass and heat exchange at the bubble wall

The evaporation-condensation process and diffusion of the noble gas into the surrounding liquid are included. The net evaporation rate (mass per unit area and unit time) at the bubble wall is given as follows [16, 18]

$$\dot{m}_e = \frac{\alpha_M}{\sqrt{2\pi R_v}}\left(\frac{P_{\rm sat}(T_{l,\rm int})}{\sqrt{T_{l,\rm int}}} - \frac{\Gamma P_{v,\rm int}}{\sqrt{T_{v,\rm int}}}\right), \tag{15}$$

where α_M is the accommodation coefficient that shows which portion of water vapor molecules hitting the liquid surface is absorbed by this interface, R_v is the gas constant of water vapor, $P_{\rm sat}$ is the saturation vapor pressure at liquid temperature $T_{l,\rm int}$, $P_{v,\rm int}$ is the partial pressure of water vapor, and Γ is the correction factor:

$$\Gamma = \exp(-\Omega^2) - \Omega\sqrt{\pi}\left(1 - \frac{2}{\sqrt{\pi}}\int_0^{\Omega}\exp(-x^2)dx\right), \tag{16}$$

$$\Omega = \frac{\dot{m}_e}{P_{v,\rm int}}\sqrt{\frac{R_v T_{v,\rm int}}{2}}. \tag{17}$$

In this study, the jump of temperature across the interface is assumed zero, thus $T_{l,\rm int} = T_{v,\rm int}$, and the accommodation coefficient is calculated as in [18]. Although Eq. (15) is valid only below a critical point (for water $T_{\rm cr} \approx 647$ K), it is used throughout the whole acoustic cycle for simplicity.

The rate of mass diffusion of the noble gas dissolved in the liquid at the wall is

$$\dot{m}_d = 4\pi R^2 D_l \left.\frac{\partial c}{\partial r}\right|_R, \tag{18}$$

where R is the bubble radius, D_l is the diffusion coefficient of the noble gas, and c is the mass concentration of the noble gas dissolved in the liquid.

The boundary conditions of species and energy at the bubble surface are derived by balancing the flux and source/sink of an interface control volume with infinitesimal thickness. In doing so, we assume that there are no uptakes of radical species or surface reactions. The resulting boundary condition for gas species is

$$-J_i|_R + \dot{m}_{\rm tot} Y_i = \dot{m}_e f_i^e + \dot{m}_d f_i^d, \quad i = 1, \cdots N, \tag{19}$$

where

$$\dot{m}_{\rm tot} = \dot{m}_e + \dot{m}_d, \quad f_i^e = \begin{cases} 1 & i = \text{water vapor} \\ 0 & i = \text{other species} \end{cases}, \quad f_i^d = \begin{cases} 1 & i = \text{noble gas} \\ 0 & i = \text{other species} \end{cases}. \tag{20}$$

The boundary condition of energy is

$$\left[\lambda\frac{\partial T}{\partial r} - \sum_{i=1}^{N}\left(J_i - \dot{m}_{\rm tot} Y_i\right) h_i\right]_R + \dot{m}_e L - \dot{m}_d \Delta H = \lambda_l \left.\frac{\partial T_l}{\partial r}\right|_R, \tag{21}$$

where T_l and λ_l are the temperature and thermal conductivity of the liquid, respectively, L is the latent heat of evaporation of the liquid, and ΔH is the heat of solution of noble gas into the liquid [32, 39].

The gas and liquid velocities at the bubble surface and the velocity of the bubble wall differ due to mass transfer. The boundary condition for gas and liquid velocities are

$$u\mid_R = \dot{R} - \frac{\dot{m}_{\rm tot}}{\rho}, \quad u_l\mid_R = \dot{R} - \frac{\dot{m}_{\rm tot}}{\rho_l}, \tag{22}$$

The mass and heat transfer boundary conditions are nonlinear. All the boundary conditions for the gas dynamics have to be coupled with the motion, temperature and noble gas concentration equations in the surrounding liquid.

B. Motion, heat and mass transport in the liquid

The liquid flow outside the spherical bubble is accounted for with different approximations for motion and heat (or mass) transport, respectively. First, the Euler equation for the inviscid motion can be reduced to the ordinary differential equation for the bubble radius known as the RP equation. The RP equation is coupled with the NS equations through stress equilibrium condition at the bubble wall. Second, when accounting for heat and mass transfer in the liquid, we assume that the fluid is incompressible. The separate treatment reduces the complexity of solving a fully coupled hydrodynamic equations for the outer liquid at sacrifice that shock waves in the liquid can not be simulated well.

Because the mass transfer at the bubble wall results in very small liquid velocity whose effect on the RP equation can be ignored, we let $u_l|_R = \dot{R}$. Thus we can use a form of the RP equation [40, 41] that includes first order terms in the Mach number $M = \dot{R}/C_{lb}$ and allows for variable speed of sound in the water [14, 42]:

$$(1-M)\,R\ddot{R} + \frac{3}{2}\left(1-\frac{1}{3}M\right)\dot{R}^2 = (1+M)\left[H_b - \frac{1}{\rho_{l\infty}}P_s\left(t+\frac{R}{C_{l\infty}}\right)\right] + \frac{R}{C_{lb}}\dot{H}_b. \tag{23}$$

Here subscripts b and ∞ denote bubble wall and infinity respectively, $P_s(t) = -P_a\sin(2\pi f t)$ is the pressure of the sound field with frequency f and amplitude P_a. For water, an equation of state of the modified Tait form

$$\frac{P+B}{P_\infty+B} = \left(\frac{\rho_l}{\rho_{l\infty}}\right)^n \tag{24}$$

is used with $B = 3049.13$ bars and $n = 7.15$. The enthalpy H_b and the speed of sound C_{lb} of the liquid at the bubble surface are given by:

$$H_b = \int_{P_\infty}^{P_l}\frac{dP}{\rho_l} = \frac{n}{n-1}\left(\frac{P_{lb}+B}{\rho_{lb}} - \frac{P_\infty+B}{\rho_\infty}\right), \tag{25}$$

$$C_{lb}^2 = \left.\frac{dP}{d\rho_l}\right|_b = \frac{n(P_{lb}+B)}{\rho_{lb}}. \tag{26}$$

The pressure P_{lb} on the liquid side of the bubble surface is related to the pressure $P(R,t)$ on the gas side of the bubble surface by normal stress equilibrium condition

$$P(R,t) - \tau_{rr}|_{r=R} = P_{lb} + \frac{4\eta\dot{R}}{R} + \frac{2\sigma}{R} \quad , \tag{27}$$

where η is the dynamic viscosity and σ is the surface tension. Their values depend on T_l, as formulated in the Appendix of [39] and [27], respectively.

Both heat and mass transfer are taken into account although the former is found to be more important to the bubble dynamics. The equations for the water temperature and the mass concentration of dissolved noble gas take similar form:

$$\frac{\partial T_l}{\partial t} + u_l\frac{\partial T_l}{\partial r} = \frac{\lambda_l}{\rho_l C_{P_l}}\frac{\partial}{r^2\partial r}\left(r^2\frac{\partial T_l}{\partial r}\right), \tag{28}$$

$$\frac{\partial c}{\partial t} + u_l\frac{\partial c}{\partial r} = D_l\frac{\partial}{r^2\partial r}\left(r^2\frac{\partial c}{\partial r}\right), \tag{29}$$

where C_{P_l} is the specific heat at constant pressure of the liquid. In solving Eqs.(28) and (29), we assume that the liquid is incompressible so that the liquid velocity can be determined as

$$u_l = \frac{\dot{R}R^2}{r^2}. \tag{30}$$

The boundary condition for the water temperature are the continuity of heat flux Eq. (21) and $T_l\mid_{r=\infty} = T_\infty$, and the boundary condition for the mass concentration is

$$c\mid_{r=R} = \frac{c_0(T_\infty)}{P_0} P_{\rm Ar}(R,t), \quad c\mid_{r=\infty} = c_\infty. \tag{31}$$

Here c_0 is the saturated dissolved gas concentration at T_∞ and P_0, and $P_{\rm Ar}$ is the partial pressure of the noble gas on the internal side of the bubble interface.

C. Numerical method

To exploit the advantage of a stationary Eulerian meshes, we use $x = r/R(t)$ to transform the NS equations (1) to a form in fixed domain $x \in [0,1]$ as done in our earlier work [14]. The transport equations for water temperature T_l and mass concentration c in domain $r \in [R,\infty]$ are transformed into diffusion-type equations in domain $z \in [0,1]$ through two consecutive coordinate transformations [43, 44] with the aid of Eq. (30). The details were given in [14, 45].

We apply a second-order total-variational-diminishing (TVD) scheme [46] to the inviscid flux terms and central difference to the diffusive terms of the NS equations. The temporal discretization differs from [14] in that we now use an Adams-Bashforth explicit scheme for the convective and spherical coordinate terms, and Crank-Nicolson implicit scheme for diffusive and chemical source terms. The implicit treatment is to overcome the stiffness problem due to diffusive transport and chemical source terms. Trapezoidal rule and central difference are used for the water temperature and concentration equations. A predictor-corrector method is used for the RP equation. We use 400 grid points for the NS equations and 100 points for the water temperature and gas concentration equations.

III. OPTICAL POWER RADIATED BY THE BUBBLE

To see how existing popular light emission models of SBSL behave in the present hydrodynamic framework, we select the optically thin model of Hilgenfeldt *et al.* [8] and the opacity-corrected blackbody model of Ho *et al.* [11, 29]. In the later model, the bubble was intensionally divided into a blackbody core and an optically thin radiating/absorbing outer shell in a way similar to what Moss *et al.* did [10, 23]. While the assumption of a blackbody core might contradict with computed photon mean free path, it just serves to show how a blackbody model works [12]. We apply the formulae of photon absorption coefficients to the gas mixture in the bubble. The overall photon absorption coefficient $\kappa_\lambda^{\rm tot}$ is the sum of contributions from all species

$$\kappa_\lambda^{\rm tot} = \sum_{i=1}^{N} \left(\kappa_{\lambda,i}^{\rm ff+} + \kappa_{\lambda,i}^{\rm ff0} + \kappa_{\lambda,i}^{\rm bf} \right), \tag{32}$$

where $\kappa_{\lambda,i}^{\rm ff+}$ is the absorption due to the free-free interaction of electron and ions, $\kappa_{\lambda,i}^{\rm ff0}$ is the absorption due to free-free interactions of electrons and neutral atoms, and $\kappa_{\lambda,i}^{\rm bf}$ is the absorption by bound-free ionization of already excited atoms. The formulae for $\kappa_{\lambda,i}^{\rm ff+}$, $\kappa_{\lambda,i}^{\rm ff0}$, and $\kappa_{\lambda,i}^{\rm bf}$ were given in [8, 47]. The ionization potentials used can found in [48]. The bound-bound absorption is not accounted for and the modification to electron-neutral-atom bremsstrahlung [7, 49] is not adopted.

The finite opacity model (without the redundant Θ correction in [11]) is used to compute the total spectral radiance (power emitted per wavelength interval) of the bubble content at wavelength λ

$$\begin{aligned} P_\lambda^{\rm Pl}(t) \;=\; & \int_{R_c}^{R} 16\pi \kappa_\lambda^{\rm tot}(r,t) R_\lambda^{\rm Pl}(r,t) \exp\left(-\int_r^R \kappa_\lambda^{\rm tot}(r')dr' \right) r^2 dr \\ & + 4\pi {R_c}^2 R_\lambda^{\rm Pl}(R_c,t) \exp\left(-\int_{R_c}^R \kappa_\lambda^{\rm tot}(r')dr' \right) \;, \end{aligned} \tag{33}$$

where

$$R_\lambda^{\rm Pl}(T(r,t)) = \frac{2\pi h c^2}{\lambda^5} \cdot \frac{1}{\exp(hc/\lambda k_B T) - 1} \tag{34}$$

is the spectral emissive power (energy per unit time, wavelength interval, and projected surface area) with the Plank and Boltzmann constants h and k_B, and the light speed in vacuum c. The radius of the blackbody core R_c determines

whether an optically thin model or an optically thick one is actually used. If R_c=0, it is the optically thin model; if R_c is large, it is the essentially blackbody model.

R_c can be defined by the expression [23]

$$\int_{R_c}^{R} \bar{\kappa}_\lambda^{\rm tot} dr = \varepsilon_c, \tag{35}$$

where $\bar{\kappa}_\lambda^{\rm tot}$ is the wavelength-averaged absorption coefficient between 200 nm and 800 nm. (35) implies that if radiation from a spherical surface at depth R_c is damped to some extent, then radiation from further interior is completely opaque to an outside observer. If $\varepsilon_c = 1$, as generally taken [23], then R_c will always be zero for all present cases, implying fully optically thin. We intentionally use a much smaller ε_c (or equivalently, increasing $\bar{\kappa}_\lambda^{\rm tot}$ while keeping $\varepsilon_c = 1$) so that there is always a finite blackbody radius R_c for most cases.

It is meaningful to look at the light pulses and spectra. The integration of the spectral radiance over a suitable wavelength intervals ($\lambda_{\rm UV}$ = 200 nm $\sim$ $\lambda_{\rm r}$ = 800 nm) gives the total power emitted into the measurable part of the spectrum, and integration over one acoustic period T_s gives the light spectrum that can be compared with the experimental results

$$P^{\rm Pl}(t) = \int_{\lambda_{\rm UV}}^{\lambda_{\rm r}} P_\lambda^{\rm Pl}(t) d\lambda, \quad S_\lambda^{\rm Pl} = \frac{1}{T_s}\int_0^{T_s} P_\lambda^{\rm Pl}(t) dt \tag{36}$$

IV. NUMERICAL RESULTS

It is well known that the ambient bubble radius R_0 depends on experimentally controllable parameters such as the driving pressure amplitude P_a, the water temperature T_∞, the gas concentration dissolved in the water c_∞. A problem with past SL spectrum measurements was they seldom gave the key parameters P_a and R_0 at the same time. The theoretical studies had to fit experimental data using different P_a and R_0. The present study tries to use the same parameters as those in previous literatures. For comparison with other calculations, the parameters used here are P_a = 1.2 bar, T_∞ = 298 K and P_a = 1.35 atm, T_∞ = 300 K for identical equilibrium radius R_0 = 4.5 μm and driving frequency f = 26.5 kHz, and P_a = 1.4 bar for R_0 = 6.0 μm, f = 20.6 kHz, T_∞ = 293.15 K, the dissolved gas concentration is c_∞/c_0 = 0.395% (3 torr partial pressure). The former two cases, P_a = 1.2 bar and 1.35 atm correspond to computational examples in Storey [22] and Xu [28], while the third case P_a = 1.4 bar corresponds to that in Moss [23]. For comparison with experiments [12], R_0 = 4.5 μm (He), 5.5 μm (Xe), f = 42 kHz, T_∞ = 296.15 K, noble gas dissolved at 150 torr (He), 3 torr (Xe), while P_a is adjustable. Other parameters are: P_∞ = 101325 Pa, $\rho_{l\infty}$ = 996.6 kg m^{-3}, k_l = 0.609 W m^{-1} K^{-1} and $C_{{\rm P}l}$ = 4179 J kg^{-1} K^{-1}, $D_l = 2\times10^{-9}$ m^2/s. The van der Waals excluded volumes are given in Table I. Initial number densities of ions and electrons are estimated using the Saha equation [47]. The initial bubble content contains 2% molar fraction water vapor. This number seems arbitrary, but our results are based on the second acoustic cycle when initial disturbances are presumed to be decayed.

TABLE I: van der Waals excluded volumes.

Species	He & ions	Ar & ions	Xe & ions	H_2O	OH	H	H^+	O	O^+	H_2	O_2	e^-
$\tilde{b}_i$ (cm^3/mol)	23.7	32.2	51.0	30.5	15.25	4.98	36.8	2.77	27.7	26.6	31.8	0.0

A. Effects of chemical reactions

Fig. 1 shows one forcing period of the radius of an argon bubble corresponding to cases I to III in [22]. One can see that the difference between II and III are small, but the difference between I and the latter two is large. The existence of water vapor increases the maximum radius and delays the collapse. In spite of little difference between II and III in $R-t$ curves, large difference occurs for thermodynamic variables at collapse. Table II shows comparison of some quantities. The maximum radius of the present calculation is smaller than that of Story [22]. This is mainly because the acoustic forcing terms in Eq.(23) is separate from H_b rather than absorbed in P_∞ as treated in [22, 33] that magnified P_a by a factor of $n/(n-1)$ (see Eq.(25)). Since there are much differences between the present model and Storey's, quantitative discrepancies are expectable for the extreme values. Both models predicted temperature reduction from case I to III. However, the present result show that temperature is slightly reduced from I to II,

but heavily from II to III. The slight reduction is due to the compensating effects of increased compression ratio ($R_{\max}/R_{\min}$) and reduced ratio of specific heats [22]. The larger reduction from 17000 K (case II) to 8900 K (case III) indicates the significant effects of chemical reactions of the trapped water vapor.

TABLE II: Comparison of extreme values for an argon bubble $R_0 = 4.5$ μm, $P_a = 1.2$ bar. The amount of water vapor is the value at $R_{\min}$ and is in mole fraction.

	$R_{\max}/R_{\min}(\mu\text{m})$		$T_{\max}$ (K)		total vapor (%)	
case	present	Ref. [22]	present	[22]	present	[22]
I	25.4/0.88	28.0/0.80	17900	20900		
II	28.7/0.76	31.3/0.70	17000	9700	7.7	14
III	28.9/0.70	31.7/0.65	8900	7000		

The effects of chemical reactions on thermodynamic variables are best reflected in the distributions of temperature and chemical yields inside the bubble. Fig. 2 shows snapshots of the spatial profiles of temperature around the moment of minimum bubble radius. It can be seen that temperatures are considerably reduced in the bubble interior in the reacting case III. Fig. 3 shows the numbers of molecules of different species and temperature at the bubble center as a function of time around the instant of minimum bubble radius. Note that in the first acoustic cycle the water vapor begins to dissociate appreciably at $t = -2 \sim -1$ ns, while in the beginning of the second cycle there are already some amounts of H_2 and O_2 gases accumulated. The chemical reactions occur in a time scale of several nanoseconds, producing considerable amounts of H, O, OH radicals and H_2 and O_2 gases. It is remarked that the prediction of chemical products is very difficult as the reaction mechanisms and phase change processes are largely unknown under extreme conditions in a SL bubble.

Next we compare a $R_0 = 6.0$ μm Ar bubble driven at $P_a = 1.4$ bar. This case was labelled as A1 in [23]. The present temperatures at the bubble center are 109600 K, 34700 K, and 16200 K for the three cases similar to I $\sim$ III in Fig. 1, thus it is seen that both the reduced ratio of specific heats due to the presence of water vapor and the chemical reactions contribute significantly to the reduction of temperatures for this higher P_a case. The amount of trapped water vapor at the moment of $R_{\min}$ for case II occupies 23% molar fraction, smaller than 33 % [22]. Fig. 4 shows several snapshots of the spatial profiles of thermodynamic variables around the moment of minimum bubble radius. A main feature in Fig. 4 is that only compression waves occur. As seen from the velocity profile, a compression wave moves outward at t_4 and t_5, reflects from the bubble wall and moves inward at t_6. No shock waves are developed. This result is different from that of Moss *et al* [23], where shock waves were reported. Possible reason is that the formation of a shock is sensitive to differences in equations of state, accommodation coefficients, chemical reactions, and treatments of the liquid motion and so on. Another feature in Fig. 4 is that temperature in the inner zone of the bubble is reduced more severely than in the outer zone at t_1, t_2, t_7 and t_8 when the compression wave is not strong. This is because considerable water vapor is trapped in the inner zone of an Ar bubble as a result of thermal diffusion [28, 33] and reacts there, thus peak temperature is not at the center, but at some place close to the bubble interface. For a lighter-than-water-vapor gas bubble such as He bubble, less water vapor is congregated in the central zone, and temperature peak will be located at the bubble center (will be shown in Fig. 6 (b)). Fig. 5 shows one snapshot of the number density distributions at the moment of minimum bubble radius. It can be seen that the amounts of products due to chemical reactions are ten orders of magnitude larger than those due to ionizations, and the number densities of H^+ and O^+ exceed that of Ar^+. Therefore, the degrees of ionization is quite low, which is in contrast to our earlier results when water vapor was not taken into account [11].

The comparative study in this subsection demonstrates that the trapped water vapor and ensuing endothermic chemical reactions significantly reduce the temperature, and that the number densities of typical ions are very small. This suggests that a few percent degree of ionization is not likely to occur in an Ar bubble. Regardless how actually the degree of ionization will be, the chemical reactions of water vapor can produce considerable amounts of radicals and molecular species, some of which such as H and O atoms are easier to ionize than a noble gas such as He or Ar. This has significant impact on SBSL mechanism as will be shown in subsection C.

B. Effects of noble gas types

Previous numerical studies pointed that shock formation depends sensitively on, among other factors [14], the amount of water vapor [23, 28] and its distribution [22]. Xu *et al.* [28] showed that shock waves develop in a bubble filled with 70% Xe and 30% (mole fractions) water vapor, but no shocks occur for similarly filled Ar or He bubbles. With evaporation-condensation process and chemical reactions taken into account, we are able to investigate effects

of noble gases on the thermodynamic processes more realistically. We calculated Xe, Ar and He bubbles using the same R_0, P_a, f, and T_∞ as those of Xu [28].

Fig. 6(a) and (b) show snapshots of the spatial profiles of thermodynamic variables around the moment of minimum bubble radius for Xe and He bubbles. Snapshots of Ar bubble are similar to those in Fig. 4, thus are not shown here. In Xe bubble (Fig. 6(a)), it is seen that an inward-going compression wave at t_2 evolves into a strong outward-going shock at t_3. It is found that the first focusing of the shock happened between t_2 and t_3 leads to extreme high temperatures ($> 10^6$ K), but the duration is very short (< 1 ps) and the region is confined to the center ($r < 0.005$ μm). On the other hand, Fig. 6(b) shows that only weak compression waves occur in He bubble. Therefore, the present result indicates that shock waves occur in Xe bubble, in agreement with Xu *et al.*'s result. Note that the temperature peaks are often at the center in He bubble except when a wavy disturbance reflects from the bubble wall at t_4. This feature results mainly from the thermal diffusion between the noble gas and the water vapor.

Fig. 7(a) and (b) show one snapshot of the number density distributions at the moment of minimum bubble radius for Xe and He bubbles. There are significant amounts of chemical products for both bubbles, especially H, O, OH, and H_2. The right figure in Fig. 7(a) shows that atoms in Xe bubble are ionized appreciably in a very small zone ($r < 10\%R$). However, Fig. 7(b) shows that the amounts of ion species in He bubble are as little as the orders of the fluctuating numerical roundoff errors. The number density of H^+ or O^+ is comparable to that of Xe^+, but far exceeds that of He^+. The situation for Ar bubble is found to be in between. The gradually increased portions of trapped water vapor (both in number density and mass fraction) from Xe, Ar to He bubbles, indicate that the chemical products from water vapor, most probably H and O, may play an increasingly important role in SBSL from Xe to He bubbles.

C. Calculated light spectra and pulses

In this subsection, we shall compute the emitted lights by using (33) with $\varepsilon_c = 1$ for the optically thin model and a smaller, adjustable ε_c for the essentially blackbody model. We compare our calculations with Fig. 2 of a recalibrated experiment [12]: $R_0 = 4.5$ μm (He) and 5.5 μm (Xe), $f = 42$ kHz, $T_\infty = 296.15$ K, noble gases dissolved at 150 torr (He) and 3 torr (Xe). We let driving pressure amplitude P_a and ε_c in (35) be fitting parameters.

Fig. 8 shows comparison of the spectral radiances. It is seen that the essentially blackbody matches well with the experimental spectrum of Xe bubble, but the optically thin model does not so. The fitting $P_a = 1.28$ atm of the essentially blackbody is within the stable SBSL range, while the fitting $P_a = 1.55$ atm of the optically thin model seems to be out of the stable range. For the former, only a weak compression wave occurs, and the maximum temperature is 8600 K, while for the latter, a shock wave appears and the maximum temperature can be 9.4×10^5 K. However, it can be seen that either models are unable to fit the spectrum of He bubble. The essentially blackbody seems better than the optically thin model as the latter deviates far from the experiment. The blackbody fitting at $P_a = 1.45$ atm results in a maximum temperature of 16700 K, while the optically thin fitting at $P_a = 2.0$ atm results in a one of 53000 K.

Fig. 9 compares the time variations of the normalized power for the "measurable", "UV" (300-400 nm) and "red" (590-650 nm) wavelength intervals [4]. Both light emission models show good wave-length independence of light pulse, a key ingredient of SBSL thought by several researchers [4, 8]. The essentially blackbody model gives a FWHM of 185 ps for Xe bubble, and 18 ps for He bubble. On the other hand, the optically thin model gives a FWHM of 26 ps for Xe bubble, and 13 ps for He bubble. The experimental flash widths are 200 ps (Xe) and 100 ps (He) [12]. Again, it is seen that the light pulse width of Xe bubble could be approximately fit by the blackbody model, while that of He bubble could not. Fig. 10 shows the variations of the blackbody core and bubble radius with time. One can see that the blackbody core appears, attains maximum at the moment of minimum bubble radius, and disappears.

Fig. 11(a) and (b) show the total visible light powers of the blackbody model versus time for Xe and He bubbles. An important feature is that the chemical products contribute dominantly to the total power for He bubble, and considerably for Xe bubble, which is suggested by the gap between the total power and the contribution from the noble gas and water vapor. Particularly, H and O radicals are found to be dominant for the light power of He bubble. The numerical results seem to support previous postulation that light emission from radicals generated from water vapor dissociation may dominate SBSL in He bubble in water [8]. However, it must be noted that the predicted spectrum and pulse width for He bubble by using both models do not agree well with the experimental ones.

The failure of the thermal radiation model to match with the experiment as using the faithfully computed photon absorption coefficients and the improvement as using an assumed blackbody core raise contradiction. The bubble interior was found to be optically thin based on the computed photon absorption coefficient. What could be conjectured was if there existed an unknown mechanism that would increase the photon absorption coefficient of the highly compressed bubble content [3, 12]. It may be possible in some way to obtain a partially blackbody zone. One way is to have better theories to compute the photon absorption coefficients of a very dense gas mixture. Other ways resort to reducing hydrodynamic modelling uncertainties. These uncertainties include: (i) the evaporation-

condensation process, which affects the trapped amount of water vapor, (ii) the chemical and ionization processes under high pressure and high density conditions, which affects the number densities of ions and electrons, and (iii) the surrounding liquid motion, which affects how much kinetic energy is delivered to the bubble and radiated outward. Light emission processes from chemical products also need to be explored.

V. CONCLUSIONS

A refined hydro-chemical model is presented to simulate the complex processes inside a sonoluminescing bubble. The model takes into account of water vapor evaporation and condensation at the bubble wall, heat and mass transfer between the bubble and the surrounding water, and chemical reactions of water vapor and ionizations of atomic species.

The numerical simulations of Xe, Ar and He bubbles indicate that the trapped water vapor and its endothermic reactions reduce the temperature significantly. In the stable SBSL range, at most compression waves can appear in He or Ar bubbles, while shock waves can occur in Xe bubbles only for higher driving amplitudes. The lower temperature in the bubble rarely leads to appreciable ionization, except for Xe bubble at the center during the shock wave focusing. The chemical reactions of water vapor produce significant amount of radicals. These radicals become increasingly important in the light emission from Xe to He bubbles. Particularly, H and O radicals are thought to be dominant light-emitting matters.

The most noticeable result of this study is that the optically thin thermal emission model is unable to match with the experiment mainly due to the reduced temperatures in the bubble. The adoption of a modified chemical equilibrium constant for a van der Waals gas is found to raise the temperature to some extent, but not high enough to alter the above conclusion. The introduction of an optically thick region makes the calculated light spectra and pulse widths match better with the experimental for some cases. The present expertise to define an optically thick region is only meant to show potential improvement of theories in this direction. Remedies to achieve blackbody effects, such as reduction of modelling uncertainties and perhaps correction to the absorption coefficient under the extreme conditions of sonoluminescence, are worthy of further investigation.

Acknowledgments

The author thanks M. C. Chu and Yu An for meaningful discussions. This work is supported by National Natural Science Foundation of China (G10172089) and State Key Program for Developing Basic Sciences (G1999032801).

---

[1] Gaitan D., Crum L., Roy R., and Church C., J. Acoust. Soc. Am. **91**, 3166 (1992).
[2] Barber B., Hiller R., Löfstedt R., Putterman S., and Weninger K., Phys. Rep. **281**, 65 (1997).
[3] Brenner M., Hilgenfeldt S., and Lohse D., Rev. Mod. Phys., **74**(2), 425 (2002).
[4] Gompf B., Günther R., Nick G., Pecha R., and Eisenmenger W., Phys. Rev. Lett. **79**, 1405 (1997).
[5] Hiller R., Putterman S. and Weninger K., Phys. Rev. Lett. **80**, 1090 (1998).
[6] Moran M. and Sweider D., Phys. Rev. Lett. **80**, 4987 (1998).
[7] Hammer D. and Frommhold L., Phys. Rev. Lett. **85**, 1326 (2000).
[8] Hilgenfeldt S., Grossmann S., and Lohse D., Phys. Fluids **11**, 1318 (1999). We note that the term "vacuum permeability" denoted as ϵ_0 in this reference as well as in [11] should be the "vacuum permitivity" to be consistent with [47].
[9] Hilgenfeldt S., Grossmann S., and Lohse D., Nature **398**, 402 (1999).
[10] Moss W., Clarke D., and Young D., Science **276**, 1398 (1997).
[11] Ho C Y., Yuan L., Chu M.-C., Leung P T., and Wei W., Phys. Rev. E **65**, 041201, (2002).
[12] Vazquez G., Camara C., Putterman S., and Weninger K., Opt. Lett. **26**, 575-577 (2001).
[13] Vuong V. and Szeri A., Phys. Fluids **8**, 2354 (1996).
[14] Yuan L., Cheng H Y., Chu M-C. and Leung P T., Phys. Rev. E **57**, 4265 (1998).
[15] Cheng H Y., Chu M-C., Leung P T., and Yuan L., Phys. Rev. E **58**, R2705 (1998).
[16] Fujikawa S. and Akamatsu A., J. Fluid Mech. **97**, 481 (1980).
[17] Karmath V., Prosperetti A., and Egolfpoulos F., J. Acoust. Soc. Am. **94**,248 (1993).
[18] Yasui K., Phys. Rev. E **56**, 6750 (1997).
[19] Gong C. and Hart D., J. Acoust. Soc. Am. **104**, 2675 (1998).
[20] Suslik S., Didenko Y., Fang M F., Hyeon T., Kolbeck K., McNamara, W., Mdleleni M., and Wong M., Phil. Trans. R. Soc. Lond. A **357**, 335 (1999).
[21] Sochard S., Wilhelm A., and Delmas H., Ultranson. Sonochem. **4**, 77 (1977).

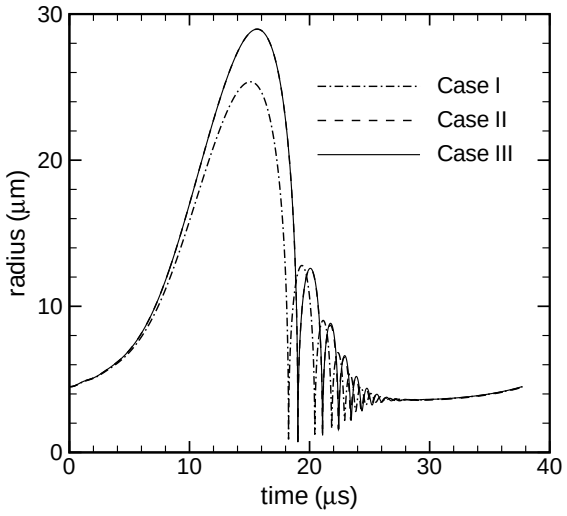

FIG. 1: Radius of an argon bubble vs. time over one acoustic period for the same parameters as used in [22]: $R_0 = 4.5$ μm, $P_a = 1.2$ bar, $f = 26.5$ kHz, $T_\infty = 298$ K. Case I: no phase change and chemistry, Case II: with phase change but no chemistry, case III: with phase change and chemistry.

[22] Storey B. and Szeri A., Proc. Roy. Soc. London A **456**, 1685 (2000).
[23] Moss W., Young D., Harte J., Levatin J., Rozsnyai B. , Zimmerman G., and Zimmerman I., Phys. Rev. E **59**, 2986 (1999).
[24] Tögel R., Gompf B. , Pecha R., and Lohse D., Phys. Rev. Lett. **85**, 3165 (2000).
[25] Tögel R., Hilgenfeldt S., and Lohse D., Phys. Rev. Lett. **88**, 034301 (2002).
[26] Xie C C., An Y., and Ying C F., Acta Physica Sinica, **52**(2), 102-108, 2003.
[27] Akhatov I., Lindau, O., Topolnikov A., Mettin, R. Vakhitova, N., and Lauterborn, W., Phys. Fluids **13**(10), 2805 (2001).
[28] Xu N., Apfel R., Kong A., Hu X W., and Wang L., Phys. Rev. E. **68**, 016309 (2003).
[29] Ho C Y., Yuan L., Chu M.-C., Leung P T., and Wei W., Europhys. Lett. **56**, 891 (2001).
[30] Poinsot T. and Veynante D., *Theoretical and numerical combustion*, R.T. Edwards, Inc. (2001).
[31] Hirschfelder J., Curtiss C., and Bird R., *Molecular theory of gases and liquids*, Wiley, New York, (1954).
[32] Reid R., Parusnitz J., and Sherwood T., *The properties of gases and liquids*, 3rd ed., McGraw-Hill, New York (1977).
[33] Storey B. and Szeri A., J. Fluid Mech. **396**, 203 (1999).
[34] Gupta R., Yos J., and Thompson R., "A review of reaction rates and thermodynamic and transport properties for the 11-species air model for chemical and thermal nonequilibrium calculations to 30000 K", NASA TM 101528, 1989 (unpublished).
[35] Wu C C. and Roberts P., Phys. Rev. Lett. **70**, 3424 (1993).
[36] GRI-Mech 3.0, http://www.me.berkeley.edu/gri_mech/
[37] Evans J. and Schexnayder J., AIAA J. **18**(2), 188 (1980).
[38] Xu N., Wang L., and Hu X W., Phys. Rev. Lett. **83**, 2441 (1999).
[39] Yasui K., J. Phys. Soc. Japan **65**, 2830 (1996).
[40] Keller J. and Miksis M., J. Acoust. Soc. Am. **68**,628 (1980).
[41] Prosperetti A. and Lezzi A., J. Fluid Mech. **168**, 457 (1986).
[42] Kamath V. and Prosperetti A., J. Acoust. Soc. Am. **85**,1538 (1987).
[43] Plesset M. and Zwick S., J. Appl. Phys. **23**, 95 (1952).
[44] Grosh C. and Orszag S., J. Comput. Phys. **25**, 273 (1977).
[45] Hilgenfeldt S., Lohse D., and Brenner M., Phys. Fluids **8**, 2808 (1996).
[46] Yee H C., "A class of high-resolution explicit and implicit shock-capturing methods", NASA TM 101088, 1989 (unpublished).
[47] Zeldovich Y. and Raizer Y., *Physics of shock waves and high-temperature hydrodynamic phenomena*, Vol. I, ed. W. D. Hayes and R. F. Probstein, Academic Press, New York (1966).
[48] Brown S C., *Basic data of plasma physics*, MIT Press, Cambrige (1966).
[49] Frommhold L., Phys. Rev. E **58**, 1899 (1998).

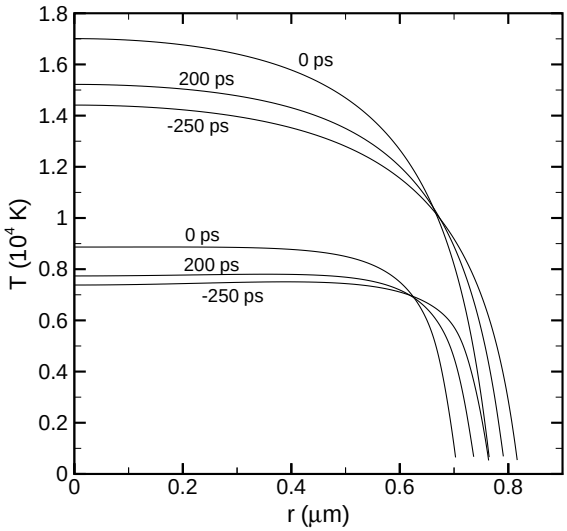

FIG. 2: Snapshots of the temperature distributions for Ar bubble at $P_a = 1.2$ bar, $R_0 = 4.5$ μm. The upper three lines are for non-reacting case II, and the lower three lines are for reacting case III. $t = 0$ corresponds to the time of minimum radius ($t_{\min} = 19.015945$ μs).

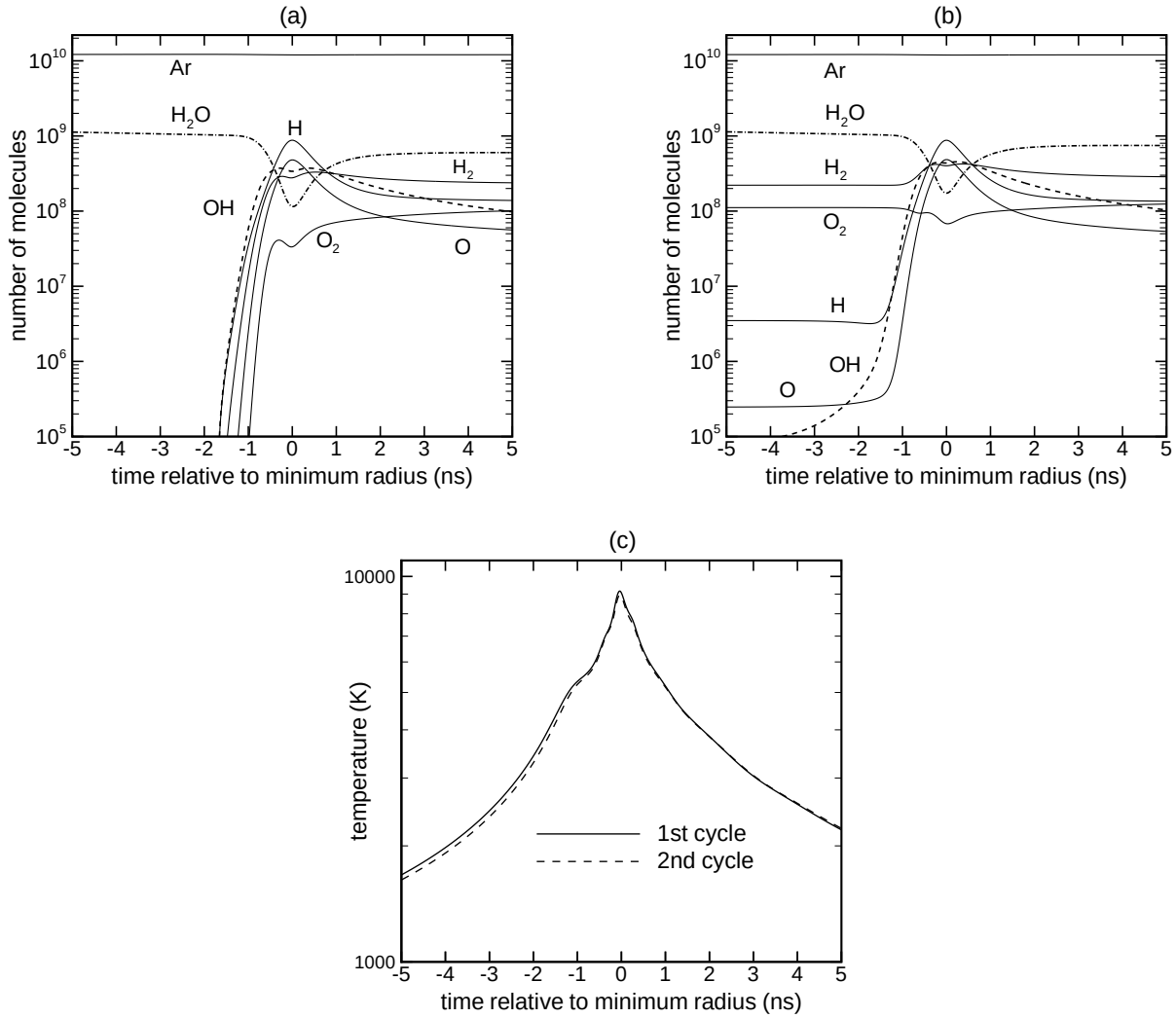

FIG. 3: The numbers of molecules of species and the temperature of the center around the moment of minimum bubble radius as a function of time for Ar bubble at $P_a = 1.2$ bar, $R_0 = 4.5$ μm. (a) first acoustic cycle, (b) second acoustic cycle, (c) temperature at the bubble center.

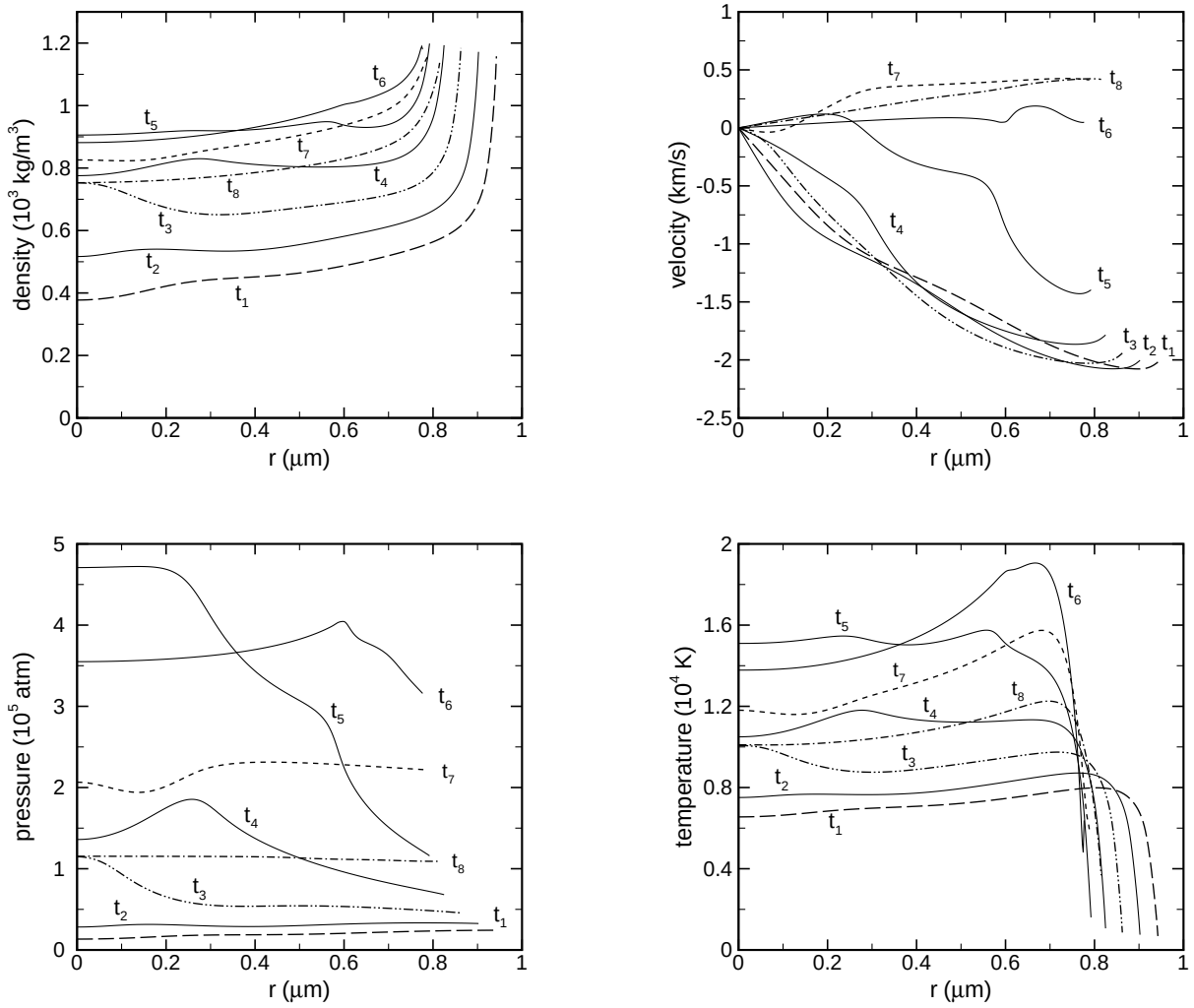

FIG. 4: Snapshots of the spatial profiles of density, velocity, pressure and temperature for $P_a = 1.4$ bar, $R_0 = 6$ μm. Time sequences are $t_1 = -100$ ps, $t_2 = -80$ ps, $t_3 = -60$ ps, $t_4 = -40$ ps, $t_5 = -20$ ps, $t_6 = 0$ ps, $t_7 = 40$ ps, $t_8 = 100$ ps, where $t_6 = 0$ denotes the time of minimum radius ($t_{\min} = 28.970309$ μs).

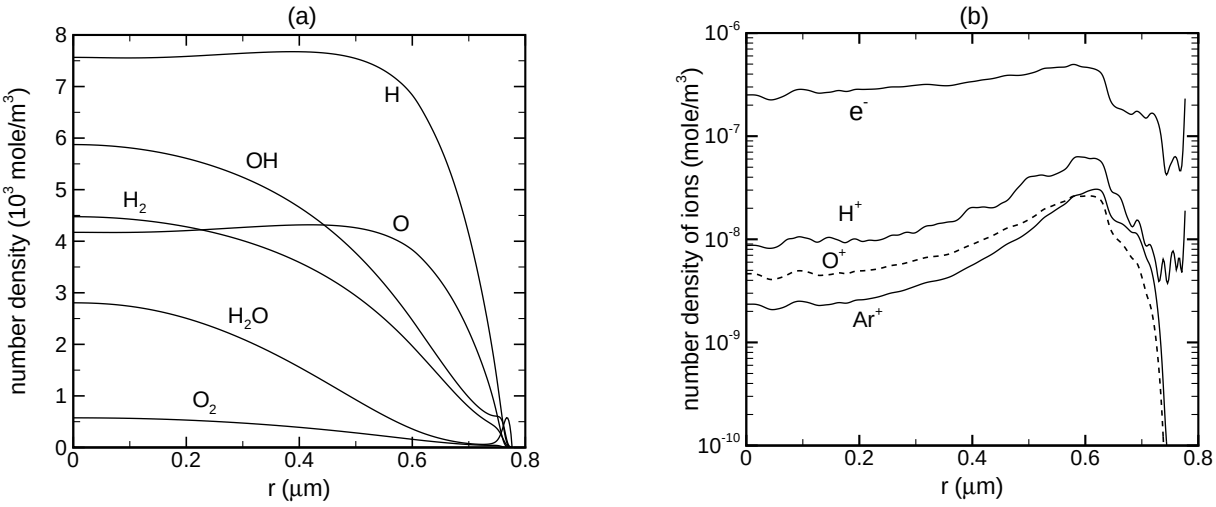

FIG. 5: The spatial profiles of number densities of (a) molecular species and (b) ion species at the time of minimum bubble radius $t = 0$ ($t_{\min} = 28.970309$ μs) for $P_a = 1.4$ bar, $R_0 = 6$ μm.

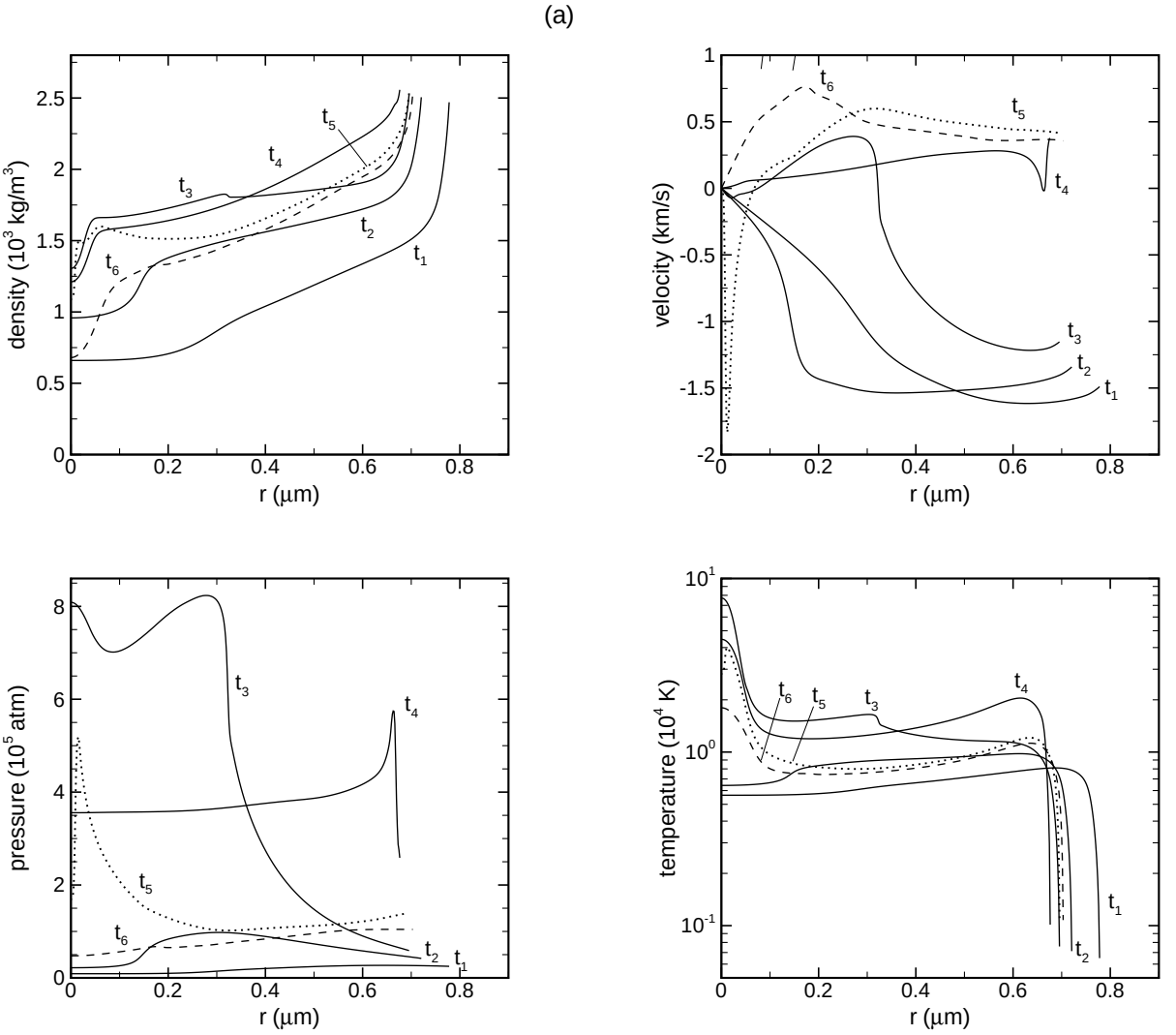

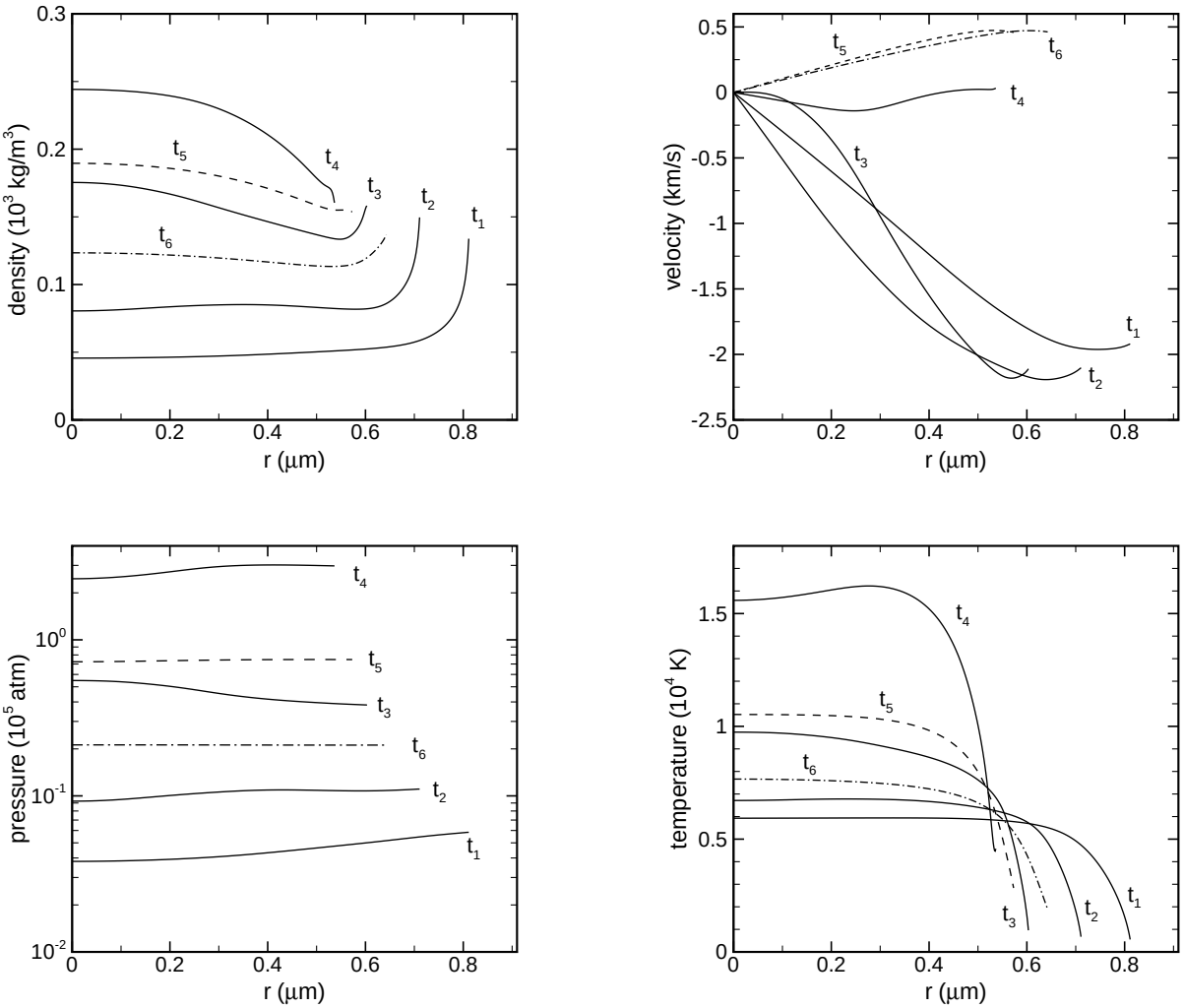

FIG. 6: Snapshots of the spatial profiles of density, velocity, pressure and temperature for $P_a = 1.35$ atm, $R_0 = 4.5$ μm. (a) Xe bubble. Time sequences are $t_1 = -80$ ps, $t_2 = -40$ ps, $t_3 = -20$ ps, $t_4 = 0$ ps, $t_5 = 40$ ps, $t_6 = 60$ ps, where $t_4 = 0$ denotes the time of minimum radius ($t_{\min} = 22.006191$ μs). (b) He bubble. $t_1 = -150$ ps, $t_2 = -100$ ps, $t_3 = -50$ ps, $t_4 = 0$ ps, $t_5 = 100$ ps, $t_6 = 250$ ps, where $t_{\min} = 22.057459$ μs.

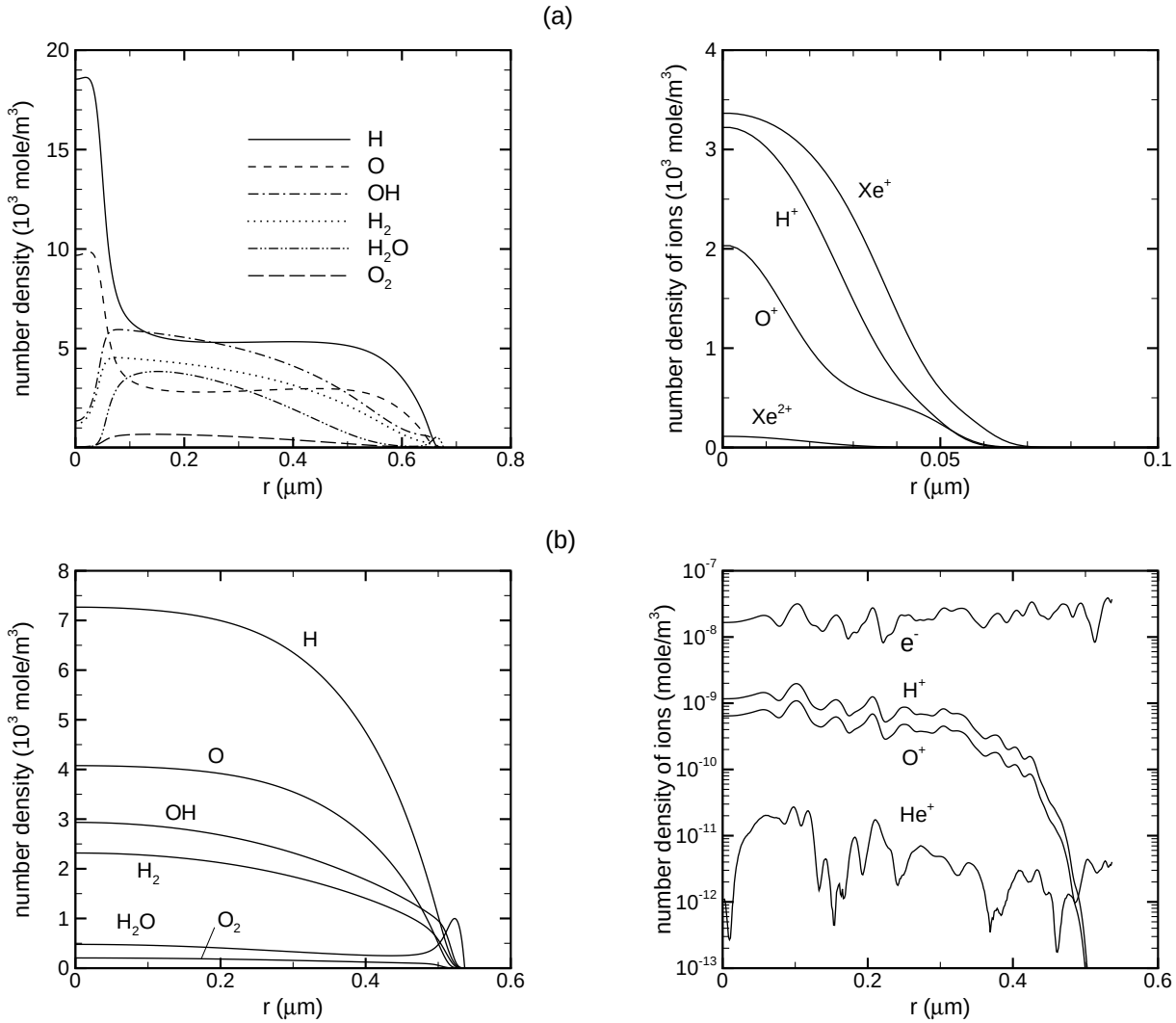

FIG. 7: The spatial profiles of the number densities for $P_a = 1.35$ atm, $R_0 = 4.5$ μm. (a) Xe bubble with molecular species (left) and ions species (right). (b) He bubble. All species are shown for the time of minimum radius $t = 0$. The small and fluctuating distributions of ions in (b) are at the numerical noise levels.

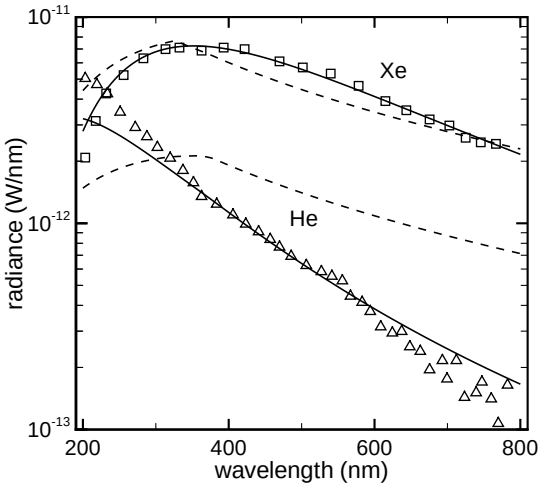

FIG. 8: Spectral radiance of the SL light from bubbles of Xe (3 torr) and He(150 torr) in water (23°C) driven at 42 kHz and. The ambient radii are the same as in experiment [12]: 5.5 μm (Xe), and 4.5 μm (He). The squares and triangles denote experimental spectra of Xe and He bubbles, respectively. The solid lines denote calculated spectra of the essentially blackbody model with fitting parameters $P_a = 1.28$ atm, $\varepsilon_c = 5.6 \times 10^{-5}$ (Xe), and $P_a = 1.45$ atm, $\varepsilon_c = 4.0 \times 10^{-3}$ (He), and the dashed lines denote that of the optically thin model with fitting parameters $P_a = 1.55$ atm (Xe) and 2.0 atm (He).

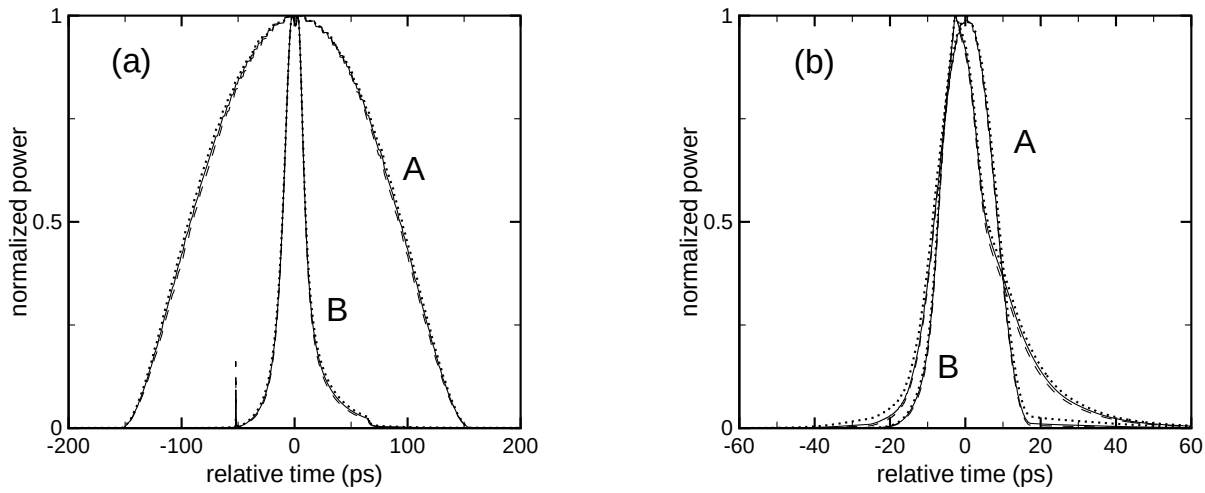

FIG. 9: Normalized radiation power vs. time for the essentially blackbody ("A") and the optically thin model ("B") in Xe bubble (a) and He bubble (b). The solid line denotes the total measurable power, the dashed line in the UV range (300 nm $< \lambda <$ 400 nm), and the dotted line in the red range (590 nm $< \lambda <$ 650 nm). Time is relative to the moment of minimum bubble radius. The parameters are the same as in Fig. 8.

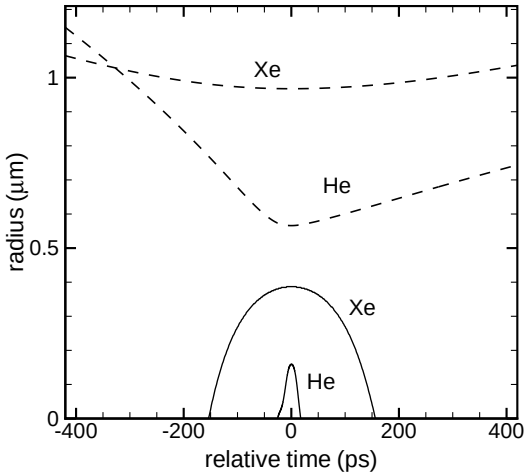

FIG. 10: The blackbody core R_c (solid line) and the bubble radius R (dashed line) vs. time for Xe and He bubbles. The parameters are the same as those for the essentially blackbody in Fig. 8.

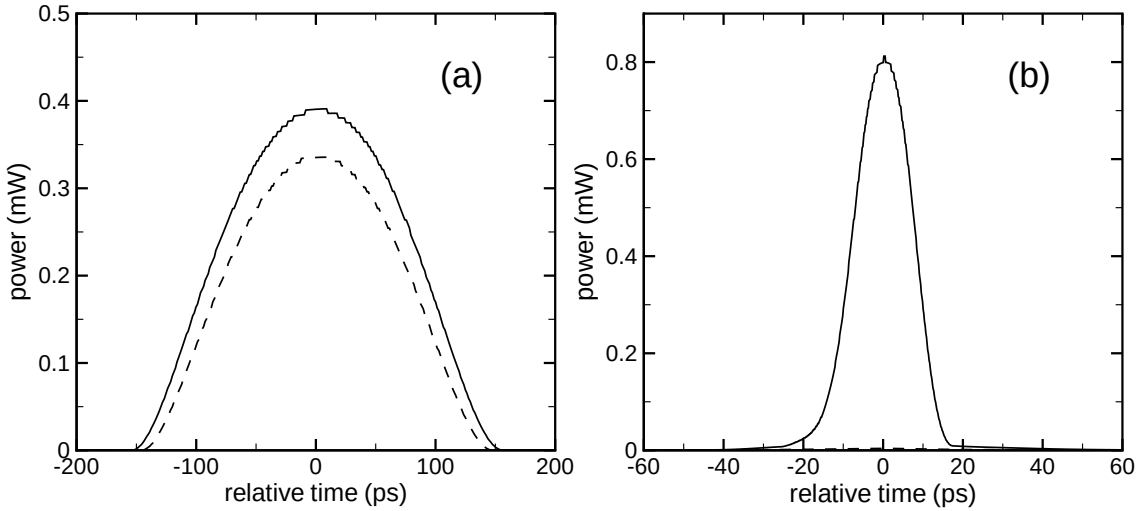

FIG. 11: Blackbody powers vs. time for Xe (a) and He (b) bubbles. The solid line denotes the total power, the dashed line in (a) denotes the contribution from noble gas and water vapor, and in (b) denotes the contribution from all species except H and O (note that it is nearly aligned with the time axis). The parameters are the same as those for the essentially blackbody in Fig. 8.